Iranian Journal of Materials Forming 7 (1) (2020) 54-69

Online ISSN: 2383-0042

IJMF

Iranian Journal of Materials Forming

Journal Homepage: http://ijmf.shirazu.ac.ir

Analysis of Cracks in the Pulsed Nd:YAG Laser Welded Joint of Nickel-Based Superalloy

M. Taheri[1*], A. Halvaee[2], S. F. Kashani-Bozorg[2] and M. Paidar[1]

[1] Department of Materials Engineering, South Tehran Branch, Islamic Azad University, Tehran, Iran
[2] School of Metallurgy and Materials Engineering, College of Engineering, University of Tehran, Tehran, Iran

ARTICLE INFO

Article history:

Received 6 September 2019
Revised 2 December 2019
Accepted 7 December 2019

Keywords:

GTD-111 superalloy
Nd:YAG laser
Solidification cracking
Liquation cracking
Grain boundary melting
Segregation coefficient
Gleeble simulation

ABSTRACT

The weldability of GTD-111 nickel-based superalloy by pulsed Nd:YAG laser welding with an average power of 250 W was studied, and the microstructural evolution and cracking characteristics were also investigated. The solidification cracking of the fusion zone (FZ) and the intergranular liquation cracking in the heat affected zone (HAZ) were observed in the joint. Solidification cracking was caused by the residual liquid metal originated from the segregation of Ti, Nb and Al elements in the interdendritic region at the last stage of solidification. And the HAZ liquation cracking was associated with the constitutional liquation of $\acute{\gamma}$, MC carbides, and the melting of Cr-rich boride. Ti was introduced as the most important factor in the formation of the liquation cracks in HAZ by reducing the start temperature of $\gamma - \acute{\gamma}$ eutectic reaction and increasing the $\acute{\gamma}$ dissolution temperature. Chemical analysis of the crack edges at HAZ revealed the presence of high amounts of Ti and Al elements which can be attributed to $\acute{\gamma}$ partial melting. Gleeble physical simulation revealed that in casting the sample, the liquation started at significantly lower temperatures than in the 1200℃ solution heat treated samples. This is attributed to the boride and intermetallic particles, which had dissolved by the 1200℃ heat treatment. The formation of fine grains due to the high cooling rate of the weld as well as the formation of dispersed carbides in the fusion and heat affected zones led to an increase in the microhardness by about 130 HV compared to the base metal.

1. Introduction

GTD-111 is a nickel-based cast superalloy which was first developed in mid 80s by General Electric Company in order to manufacture first-row gas-turbine moving blades [1]. This superalloy is known as the new generation of IN738 superalloy and modified Rene80 superalloy [2]. The GTD-111 is a modification of Rene 80 and has a multi-phase microstructure consisting of the face-centered cubic (FCC) γ matrix, bimodal γ′ precipitates (primary and secondary), γ-γ′ eutectic, carbides and a low amount of harmful phases such as σ, μ, and Laves phases [3]. The alloy obtains its high temperature strength mainly through γ′ (Ni_3(Al, Ti)) precipitates that are present with a>60% volume fraction [3].

Although their excellent mechanical properties and resistance to high temperature corrosion make them suitable for widespread use, the welding and weldability of precipitation-strengthened nickel-based superalloys have caused challenging issues for the metallurgist and metallic material researchers [4]. GTD-111 alloy, similar to other precipitation hardening superalloys which contain Al+Ti>%6, is hardly welded because of

*Corresponding author
E-mail address: mtz.taheri@gmail.com (M. Taheri)

its high sensitivity against HAZ cracking and difficult PWHT [5].

Cracking during the welding of this alloy has been attributed mostly to large shrinkage stress occurring as a result of rapid precipitation of γ' particles during cooling from the welding temperature [6]. Added to this, the non-equilibrium phase transformations and micro-segregations during non-equilibrium solidification usually result in the formation of intermetallic compounds which are rich in alloying elements that are important for strengthening. This impressively affects the high-temperature functionality of the superalloy [4].

Cracking of HAZ in nickel-based superalloys is generally caused by the presence of the liquid phase on grain boundaries at a time during which sufficient thermal and shrinkage tensile stresses are developed during the weld cooling cycle to drift apart any weak intergranular liquid-solid bonds. Careful microstructural examination revealed that liquating the microconstituents that contributed to the HAZ grain boundary liquation cracking includes MC carbides and γ' precipitates [7].

Taheri et al. [8] have introduced compounds such as γ' phase, $\gamma - \acute{\gamma}$ eutectic, MC and $M_{23}C_6$ carbides, Cr-Mo boride, and Ni-Zr intermetallic to be the main factors in the formation of HAZ liquation cracks during their investigations on laser welded GTD-111 superalloy. Presence of such compounds at the grain boundaries of nickel-based superalloys has been proven by several researchers [9, 10]. These locations are suitable locations for the nucleation and growth of cracks. Occurrence of cracks during the welding of this alloy is mainly attributed to the shrinkage stresses which are the results of the rapid precipitation of $\acute{\gamma}$ particles during cooling from the welding temperature [11]. Osoba et al. [12] have reported that HAZ cracks in Rene 80 superalloy are accompanied by grain boundary $\acute{\gamma}$ liquid. Ojo et al. [13] have shown that besides the contribution to welding stresses, γ' precipitates can embrittle weld HAZ grain boundaries by persisting to temperatures at which they could react with the austenitic γ matrix to produce a liquid phase by a eutectic type reaction.

HAZ liquation cracks are considered to be a major problem in comparison with FZ. The reason is that a FZ crack can be controlled to a great extent by the use of a suitable filler metal. Cheng and Chiang [14] have been able to decrease the weld defects such as porosities and cracks by the use of IN738 powder as a filler metal in IN738 laser welding. Ojo et al. [10] have shown that in IN738 welding with direct laser welding, there are not any solidification cracks in the weld metal, while a HAZ microstructure suffers from the presence of cracks.

The presence of secondary-phase particles in rapid heating rates can develop grain-boundary melts in HAZ [15]. Added to this, the segregation of elements with $K<1$ decreases the melting point along the grain boundaries and increases the solidification temperature range, which results in local melting and HAZ liquation cracking. The segregated elements during heating can melt during welding and produce re-solidified products. Such places are suitable sites for the nucleation and growth of cracks. The valuable point is that the presence of micro-porosities around the molten grain boundary might be a mechanism for crack formation at HAZ. Naffakh-Mosavy and Rezaei [15] have studied the effect of micro-porosities and precipitations on the crack behavior of IN718 poly-crystal. They reported that the presence of micro-porosities and laves phases at the inter-granular zones is an important source of HAZ cracks. Shrinkage cavities are formed at HAZ molten grain boundaries. These cavities are developed due to solidification shrinkage and are the results of heating/cooling cycles. Moreover, thermal expansion during welding results in the upcoming thermal stresses as well as the shrinkage strains which end in micro-porosities. Micro-shrinkage can result in hot cracking.

Solidification cracking is another mechanism that occurs during welding. Solidification cracking happens at the late solidification stages, when the molten films are being formed along the solidification grain boundaries and in some cases are distributed in the inter-dendritic sites. Equilibrium dislocation coefficient of solute element, solidification range, and strains due to the welding cycle are the most important factors which control solidification cracking. Osoba et al. [12] have suggested the segregation of elements with $K<1$ in the inter-dendritic zones, decreasing the local melting, to be the main cracking factor in FZ. Dendrite micro-segregation mainly results in the formation of secondary intermetallic solidification compounds along the inter-

dendritic zones in such a way that it ends in the non-uniform distribution of secondary-phase particles [16].

A lot of fractures in the compounds are related to the above-mentioned problems during welding. One of the most important processes that exist for repairing and joining gas-turbine blades made of GTD-111 is welding. Due to the poor fluidity of the molten weld metal for nickel-base alloys, the traditional welding method e.g. TIG fails in obtaining good penetration [17].

Laser beam welding (LBW) has been recognized as one of the most attractive welding techniques for joining advanced high temperature materials on account of its low contamination, low input heat, high welding speed (10 to 20 times TIG), low thermal deformation, high diffusivity, and better metallurgical and mechanical properties due to thin HAZ [18].

In the weldability conditions of a superalloy, the pulsed Nd:YAG laser has various advantages such as a high energy-absorption rate due to low laser beam reflection, controllability of parameters such as pulse duration, pulse frequency, as well as lower residual stresses compared with the CO_2 laser [19].

In summary, owing to the few investigations on the fusion welding of GTD-111 superalloy, it is necessary to study the laser beam weldability of GTD-111 superalloy, although there are studies using the TLP method for joining this superalloy [20]. The goal of this research was to conduct a comprehensive analysis on the microstructure of different zones and the formation mechanism of cracking defects in the joints. Finally, the tensile behavior and hardness of the alloy were studied.

2. Experimental Procedure

The material used for this study was GTD-111 nickel-based superalloy plates with a thickness of 1 mm and dimensions of 50×50 mm^2, which had totally even edges cut by a wire cut from a cylindrical ingot with a diameter of 750 mm. The chemical composition of this alloy is presented in table 1. In this study, a DSC (Differential Scanning Calorimetry) test was carried out to determine the temperature changes of GTD-111 superalloy states, such as melting and solidification, dissolution of precipitation, and carbide formation. The NETZSCH STA 409 PC/PG device was used for this purpose.

Table 1. Chemical composition of the as-cast GTD-111 Alloy (wt.%)

Cr	Co	Ti	Al	Ta	W	Mo	Nb	B	Zr	C	Ni
14	9.5	4.9	3	2.8	3.8	1.5	0.07	0.014	0.03	0.1	Bal.

Before welding, samples were cleansed in acetone solution and dried. A special fixture was used to fix the samples and maintain their positions during the welding process. Welding was autogenous and was performed by a pulsed Nd:YAG laser source model, IQL-10, with a maximum power of 400 W. Fig. 1 presents the experimental steps.

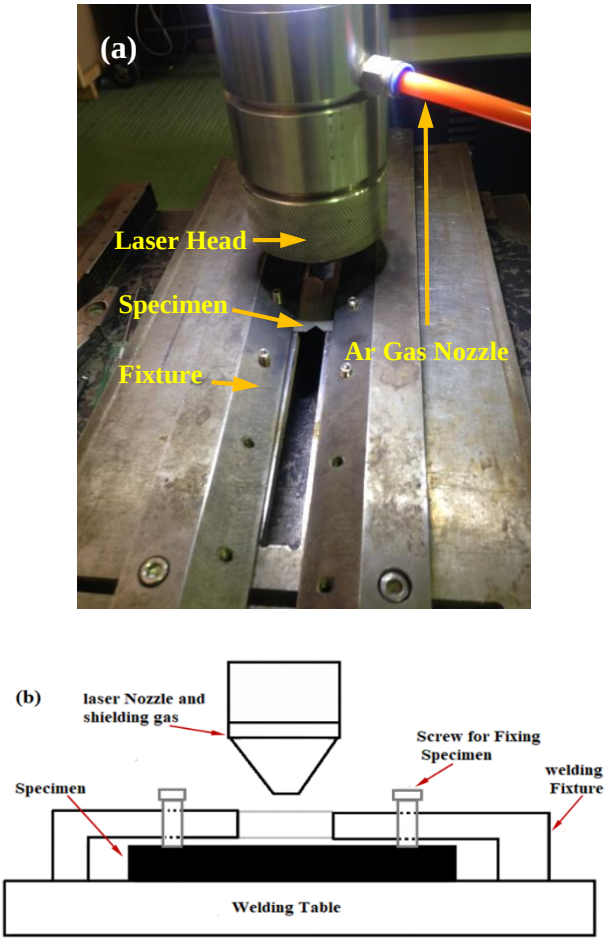

Fig. 1. Image of (a) experimental setup and (b) schematic diagram of the welding machine and work piece.

In order to obtain a suitable welding profile, the optimum parameter for welding was selected based on some previous tests and studies [21], which have been

presented in table 2. A power meter model 5000 W-Lp by Ophir was used for measuring the laser power. Fig. 2 presents the laser-welded sample. The heat affected zone microstructure of the heat-treated specimens were simulated by a Gleeble 1500-D thermomechanical simulation system to study the effect of the microstructural variation and heat treatment on the liquation behavior of GTD-111. Selected specimens were pulled to failure in order to evaluate hot ductility at various peak temperatures. The simulation was performed on the cylindrical specimens of 5 mm diameter and 85 mm length which were rapidly heated to 1050, 1140, 1170 and 1250˚C temperatures at a rate of 111 ˚C/s and then held for 1 s at all the temperatures followed by water quenching.

Table 2. Pulsed Nd:YAG laser welding parameters

Shielding gas flowrate (L min^{-1})	Heat Input (J mm^{-1})	Peak power(Kw)	Pulse Energy (J)	Average Power (w)	Speed (mm sec^{-1})	Pulse Duration (ms)	Frequency (Hz)
10	25	1.5	10.5	209	8.3	7	20

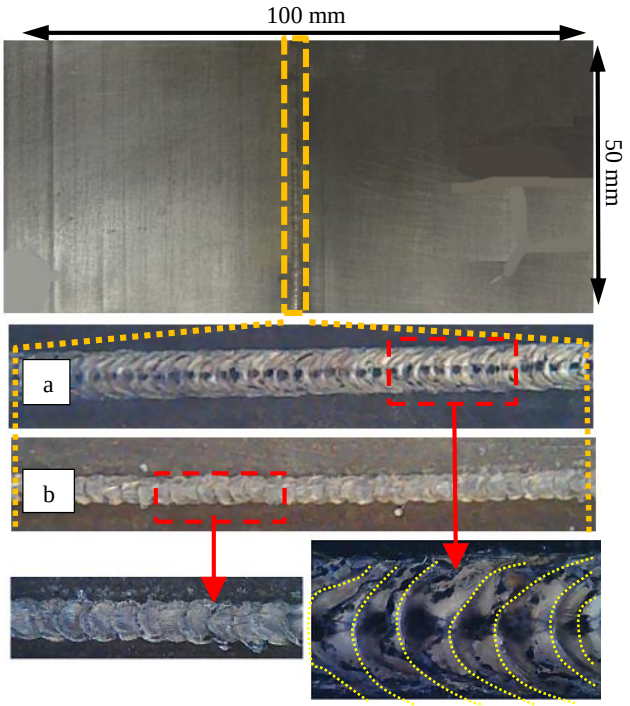

Fig. 2. Weld appearance, (a): weld appearance of the top side, (b): weld appearance of the back side.

In order to study the hot cracking behavior in HAZ, FZ and Gleeble simulation, six welded samples were cut which were taken from the cross section of the weld line using wire cut. After standard metallography, including grinding and polishing, marble etching solution having a composition of 44 g Cu_2SO_4+20 ml HCl+20 ml H_2 was used for optical microscopy studies. Electro-etching with a composition of 12 ml H_3PO_4+40 ml HNO_3+48 ml H_2SO_4 in 6 V for 5 seconds was performed with the purpose of conducting electron microscopy studies. The microstructural investigations were carried out by optical microscope (OM) as well as the field-emission scanning electron microscope (FE-SEM) model MIRA3 by TESCAN which was equipped with applicable SE, EDS, and BSE detectors. Axio Vision software was used to measure particles, especially the distance of the dendritic arms.

In order to investigate the mechanical properties of the welded metal, the microhardness test was used by Buehler equipment made in the USA with an applied load of 200 g and a time period of 20 s in the longitudinal section of the polished sample. Tensile test was performed using a Zwick/Roel Z100 machine with a Cross head speed of 2 mm/s according to the ASTM E8 standard. After the tensile testing, the fracture cross sections were investigated from a microstructural point of view. Fig. 3 shows the standard dimensions of the sample.

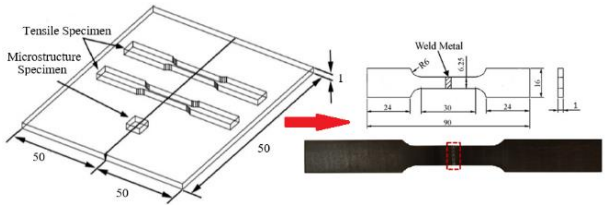

Fig. 3. Schematic diagram showing the dimensions of laser-welded specimens used in tensile tests.

3. Results and Discussion

3.1. Material microstructure before welding

Figure 4 shows the microstructure of GTD-111 base metal in as the as-cast condition. A fully developed coarse dendritic structure accompanied with severe alloying segregation in the interdendritic regions can be seen. Considering the fact that the base metal is prepared as-cast, its alloying element segregation seems normal. The dendritic core zones are observable in bright color and the inter-dendritic regions are observable in dark color. The secondary phases in the dark inter-dendritic zones as well as heavy alloying-element segregations in brighter zones, which are formed during solidification, are observable. Fig. 4(b) presents the SEM image of the base metal. As it is clear, γ, $\acute{\gamma}$, and $\gamma - \acute{\gamma}$ phases with sector morphology, and MC carbide with a size of 1.5 µm are the most important as-cast GTD-111 microstructural components. EDS analysis of the gross particles in Fig. 4(c) reveals TiC carbide particles. An intense Ta peak in the EDS pattern is a sign of (Ti, Ta) C complex carbide in the microstructure. Both γ and $\acute{\gamma}$ phases have coherent interfaces due to their possession of FCC structures and close lattice parameters. This interface is located at low-energy {100} planes. The low degree of mismatch between these two phases, results in a decrease in the driving force for the cubic nucleation and coarsening of $\acute{\gamma}$ particles, which increases the applicability of the alloy at high temperatures [2]. By growth continuation, $\acute{\gamma}$ particles convert into clusters of continuous cubes or octahedrons, and afterwards they might grow dendritically in the preferential direction of <111>.

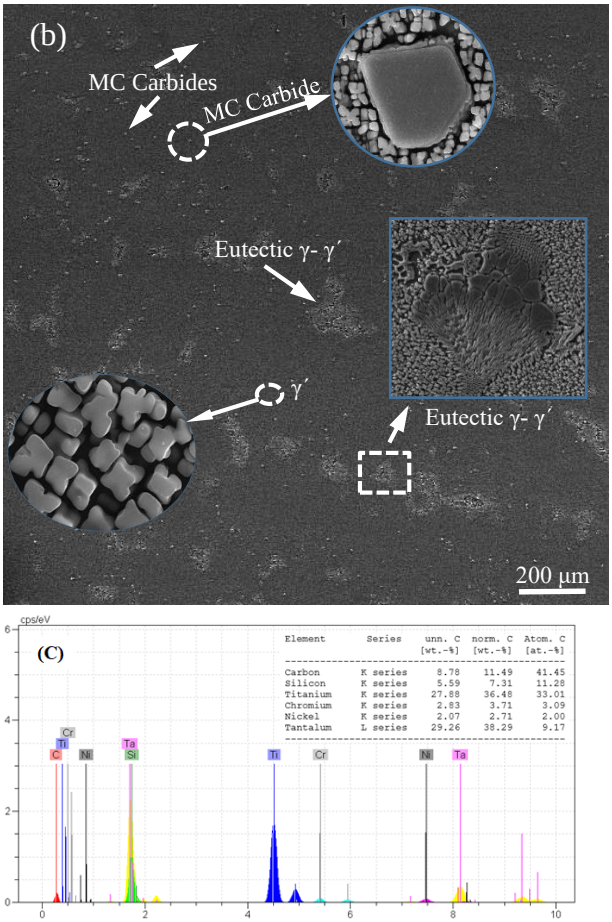

Fig. 4. as-cast base-metal microstructure: (a) optical microscopy, (b) electron microscopy, (c) carbide EDS analysis.

3.2. Weld metal microstructure

Overall, welding profile in Fig. 5 shows that the weld appearance is sound without undercuts and convexity. As can be seen in Fig. 6, the microstructure of the weld metal consists of three zones: cellular, dendritical, and equiaxed. The morphological difference between these three zones is due to their being exposed to different cooling conditions.

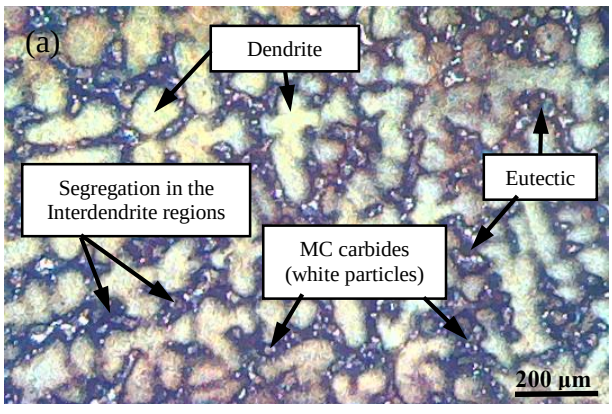

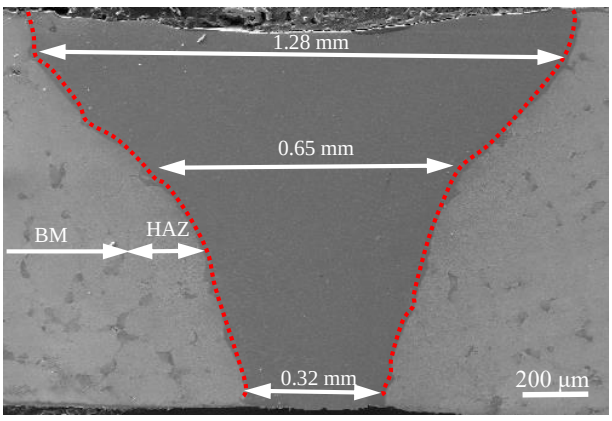

Fig. 5. Overall profile of the welded sample.

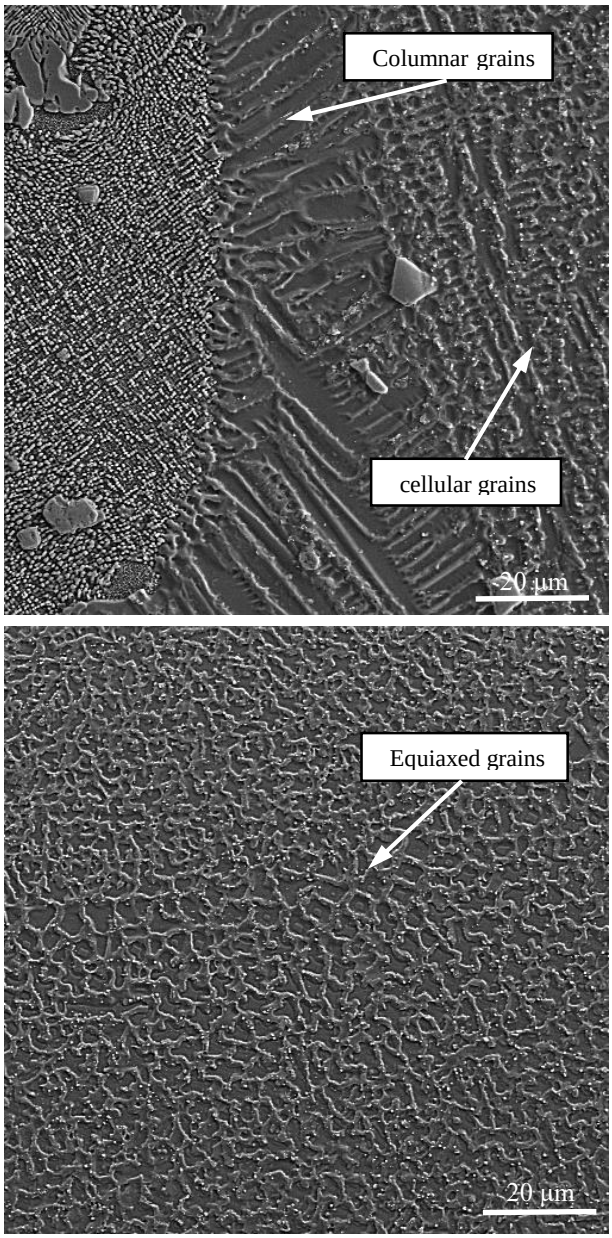

Fig. 6. GTD-111 weld metal microstructure by SEM microscopy.

The solidified microstructure is greatly affected by the solidification parameters of temperature gradient G, solidification rate R and their combinations GR and G/R. These two parameters (G and R) are responsible for these three types of structures in the weld metal which are explained by equation $\frac{G}{R} \geq \frac{-mc_0(1-K)}{KD_L}$ [22]. In this equation, G is thermal gradient, D_L is diffusion coefficient in the liquid phase, m is melt line slope, K is segregation coefficient, and R is growth rate. The units of GR and G/R are K/s and K.s/mm^2, respectively. As shown in Fig. 7, the solid-liquid interface stability factor G/R is related to the solidification morphology, while the cooling rate GR influences the scale of the solidification microstructure. As G/R increases, the interface morphology changes from equiaxed-dendritic to cellular-dendritic, and from that to cellular grains. On the other hand, dendrites of finer sizes occur under higher cooling rates. It must be noted that the high solidification and growth rates due to lower input heat are one of the characteristics of pulsed laser [23].

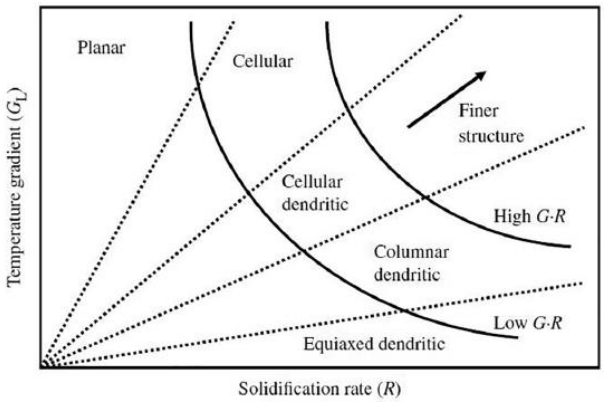

Fig. 7. The effects of the G and R on the morphology and scale of the solidified microstructure [22].

Grain crushing in FB affects the crystalline orientation of the weld metal and results in the development of an epitaxial growth zone. Epitaxial growth of the materials with more than one phase is natural. The epitaxial structure is formed in the base metal along the low energy crystalline direction. This direction in autogenous austenitic welding is <100> [22]. When the solidification mode is more affected by crystalline orientation rather than thermal gradient, the epitaxial growth stops (Fig. 8).

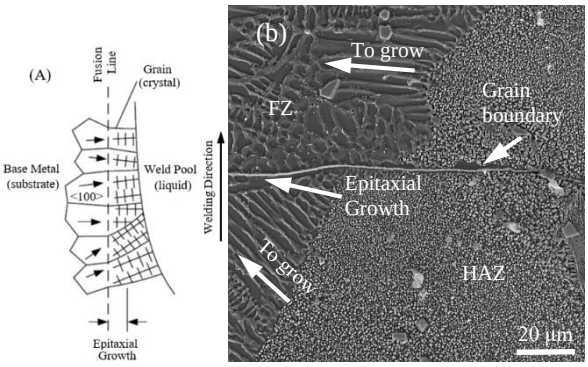

Fig. 8. Epitaxial growth of weld metal: (a) schematic, (b) SEM microscopy.

Segregation behavior of solute elements can be considerably affected by solidification growth rate. Various studies have been performed on the solidification behavior of the weld metal for nickel-based alloys using this concept [24, 25]. These studies have revealed that the redistribution behavior of solute components as well as the microstructure of the obtained weld metal is mainly controlled by the values of K and D_s for the given alloying elements. D_s controls the backward diffusion potential of the solid during solidification. A segregation coefficient k was defined as the ratio of the average concentration of the element in the dendrite cores to that in the interdendritic regions, i.e., k=Cd/Cid. K values of less than 1 (K<1) indicate that the elements segregated to the interdendritic regions and these elements are positive segregation elements, while k values of more than 1 (K>1) indicate that the elements segregated to the dendrite cores and these elements are negative segregation elements. Fig. 9 presents the X-ray map image of the weld metal microstructure for defining the distribution of different elements in the weld metal. Chemical composition of the dendritic core zones which is defined by electron probe microanalysis equipped with EPMA/WDS is presented in table 3. The results reveal that Ti, Ta, and some Al elements have segregated in the inter-dendritic zone due to their having K values of less than one. Among these, the Ti case is more severe than the other two elements. Elements such as W and Mo are distributed in the dendritic core zones due to their amount of K being more than one. The rest of the elements are almost uniformly distributed in the inter-dendritic and dendritic core zones. As the amount of C element distribution cannot be defined with sufficient precision due to its light weight, there are various studies [26] which have calculated the distribution coefficient of these elements as less than one. Therefore, it seems logical that these elements segregate during the GTD-111 welding solidification process in the inter-dendritic zones. Despite this, the presence of the distribution process during solidification is not fixed.

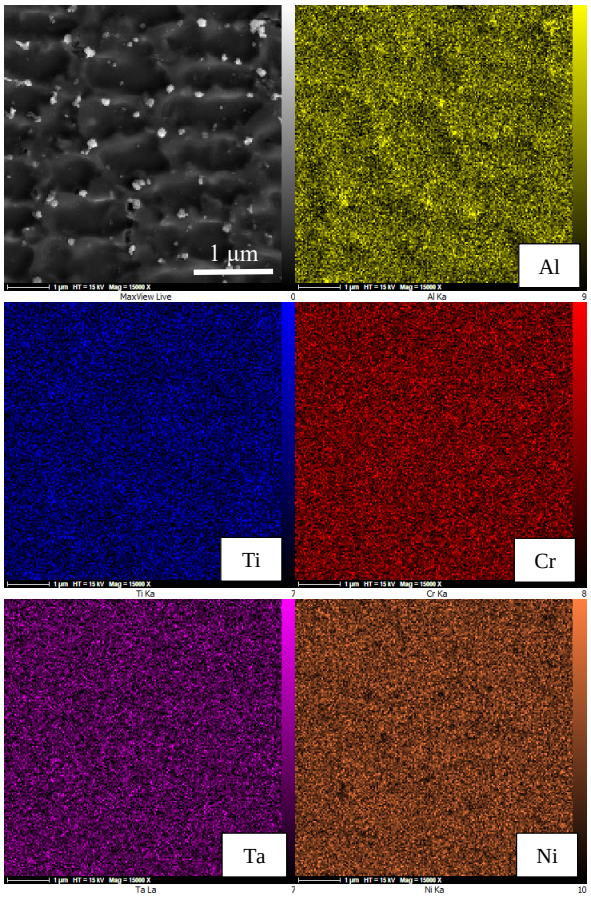

Fig. 9. EDS X-ray mapping of weld metal microstructure.

Table 3. EPMA microanalysis of interdendritic and dendritic core zones in the weld metal

Elements	Al	Ti	Cr	Mo	Co	Ni	Ta	Nb	W
Dendrite Core(C_s)	2.72	3.65	13.82	1.48	10.43	61.21	2.99	0.03	4.27
$K=C_s/C_0$	0.9	0.73	0.99	1	1.1	1.04	0.95	0.54	1.13

Based on the solidification concepts, the growth rate has a significant effect on the dendritic arm spacing as well as the redistribution degree of alloying elements in the nickel-based superalloys, which have been studied by Brody and Flemings [26] as:

$$\lambda_s = K_s R^n \quad (1)$$

In equation 1, λ_s is the average dendritic arm spacing to be about 2.2 µm. The values of K_s and n are constant, which according to references [26] are assumed to be 4.7×10^{-2} $mmk^{1/3}$ $S^{-1/3}$ and -0.4, respectively. Also, R is

the cooling rate. Based on these values, the amount of R for the welding pool of the GTD-111 nickel-based superalloy which was studied in the present work was obtained to be 2110 ks^{-1}. Such a rapid cooling rate can considerably restrict the backward diffusion potential during weld metal solidification. The works done by Giamei et al. [27] have shown that decreasing the dendritic arms has a desirable influence on decreasing segregation and increasing structure homogeneity.

$$C_s = K(C_0[1-(1-2\alpha k)f_s]^{(k-1)/(1-2\alpha k)} \quad (2)$$

$$K = \frac{C_s}{C_0} \quad (3)$$

$$\alpha = \frac{D_s t_f}{L^2} \quad (4)$$

$$t_f = \frac{\Delta T}{\partial T/\partial t} \quad (5)$$

If in equation 4, $\alpha \ll 1$, then the Brody and Fleming equation is reduced to a new equation named Scheil [28]:

$$C_s = Kc_0[1-f_s]^{(k-1)} \quad (6)$$

In the above equation K is the equilibrium solution distribution coefficient, C_o is the nominal solution concentration, f_s is the solid fraction, D_s is the solution diffusion in the solid (constant), t_f is the total solidification time, L is half the dendritic arm spacing, and α is the dimensionless diffusion parameter. Scheil equation explains the redistribution of solute components when diffusion in the solid is negligible.

The presence of brittle phases (metallurgical factor) and the simultaneous presence of stress/shrinkage (mechanical factor) are among the most important factors for the formation of solidification cracks. As seen in Fig. 10, for most of the interdendritic zones, there are cavities which have been formed during the shrinkage of liquid to solid. Accumulation of such micro-cavities results in increasing the stress concentration and as a result expanding the hot solidification micro-cracks. Enrichment of the inter-dendritic zones by segregation solutions might result in a considerable decrease in the weld metal solidus temperature. This increases the brittleness temperature range which results in the weld metal to be prone to solidification cracks. The formed cracks are mostly along the white phases which are observed in the dendritic zones.

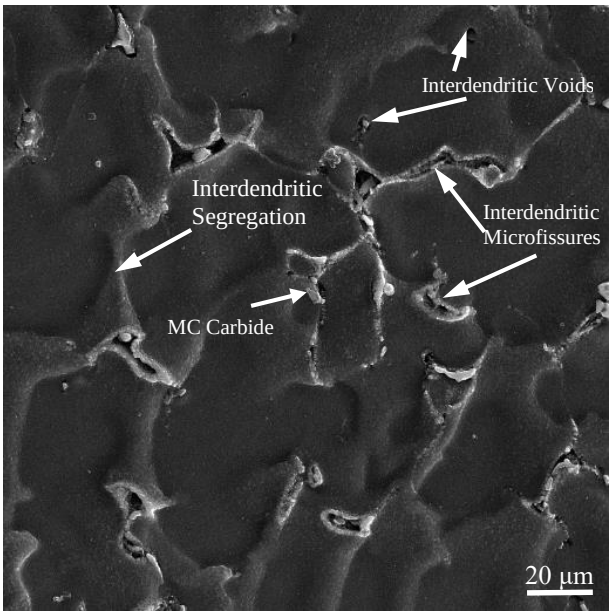

Fig. 10. Formation of cavities and cracks in the interdendritic zones of the weld metal.

Dupont [29] and Moosavy [30] developed a model based on the Scheil equation (equation 6), in which the sensitivity of nickel-based superalloys against solidification cracks can be predicted. In this equation, the relationship between K values of each X element from the weld metal and the solid fraction (f_s) with a composition of C is considered to be:

$$C_{sx} = K_x C_0 (1-f_s)^{K_x - 1} \quad (7)$$

By having K values, the nominal composition of elements as well as some other operational, physical, and microstructural parameters, solidification range of the weld metal can be used as good criteria for defining the weld ability of nickel-based superalloys.

3.3. HAZ microstructure

Figures 11(a) and 11(b) reveal signs of HAZ grain boundary melting. The re-solidified micro-cracks in this figure are attributed to the constitutional liquation of Ti and Ta rich carbides as well as the segregation of Ti, Al, and Mo elements in the grain boundaries. EDS analysis of table 4 confirms the presence of such elements. Partial melting of γ′ precipitates, which are rich in Ti and Al, is clearly visible adjacent to the side weld line in Fig. 11(b).

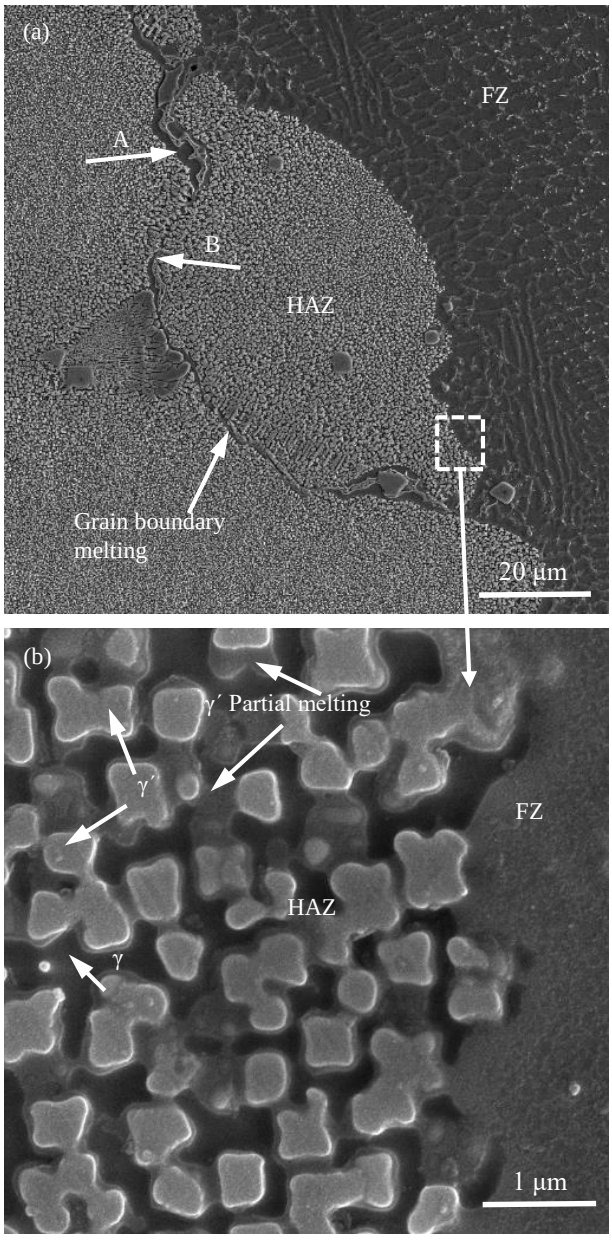

Fig. 11. (a) grain boundary melting at HAZ, (b) γ′ partial melting.

Table 4. EDS analysis of marked zones in Fig. 11(b) (at. %)

Element	Ni	Ti	Al	Cr	Ta	Co	W	Mo
A	55	29	9	2	-	3	-	-
B	8	61	2	2	14	1	3	9

According to Ojo's works [31], these precipitates can react with the γ matrix if the temperature is maintained, and a liquid phase of γ-γ′ type is formed which results in brittleness at the grain boundaries. An increase in the amount of Ti increases the γ′ solving temperature in addition to decreasing the start time of the eutectic reaction [31]. Therefore, the high concentration of Ti which is the case in the present study can facilitate the melting of γ′ through decreasing the temperature range between γ′ solution and γ-γ′ reaction temperature during welding. Fig. 12(a) and 12(b) show the formed liquation crack due to the presence of the eutectic phase at the grain boundary. Chemical analysis of the crack edges in HAZ reveals the presence of high amounts of Al and Ti in comparison with the matrix. Fig. 12(c) shows a state of cracking, in which due to the severity of cracking, the crack has been expanded up to the weld metal zone. Under such conditions and when liquid distribution is located at the grain boundaries, strength decreases and even very low stress amounts can result in HAZ liquation cracking.

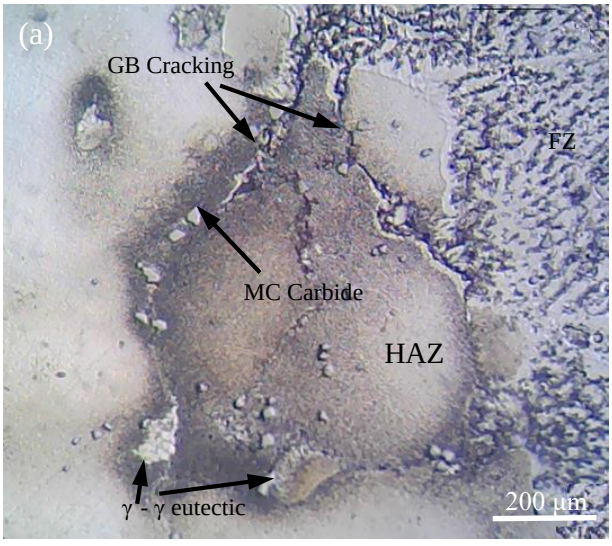

Fig. 12. Developed liquation crack at HAZ: (a) and (b) around the γ-γ′ eutectic, (c) expanded to the weld metal.

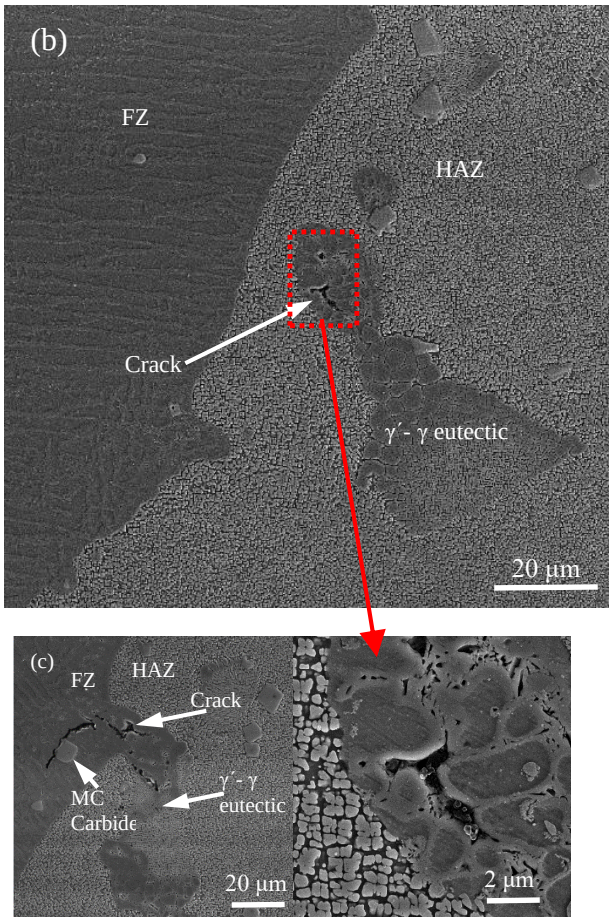

Fig. 12. Continue

3.4. Gleeble simulation of HAZ

In order to investigate the occurrence of liquation crack under the temperature of the solidus, the simulation was performed by the Gleeble thermomechanical simulation system. In this study, the experiments were carried out for two samples: (a) casting; and (b) dissolved at 1200˚C . A DSC study was first performed to determine the main equilibrium phase transformation temperatures in the GTD-111 alloy, whose results are listed in table 5 [32]. According to the above temperature table, the four peak temperatures under the Solidus temperature were selected to evaluate the starting temperature of the local melting.

Table 5. Transition Temperature for GTD-111 (ºC) [1]

γ´ Solvus	Solidus	γ´- γ Eutectic	Liquidus
1175	1295	1325	1340

The microstructure of sample B in Fig. 13(b) and (c) showed that at 1050 and 1140˚C no melting effect was observed in the samples. Only a small amount of γ' precipitation was dissolved in the simulated sample at 1140˚C. At the same time, melting did not occur for sample A at 1050˚C; however, at a temperature of 1140˚C, the melting of the γ-γ' eutectic phase could be observed partially in the structure (Fig. 13(a)).

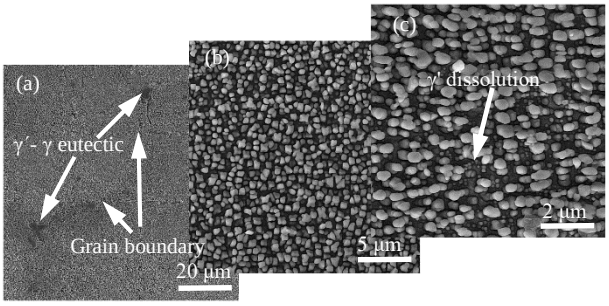

Fig. 13. Microstructure of Gleeble simulated sample at; (a) 1050˚C for sample A, (b) 1050˚C and (c) 1140˚C for sample B.

With an increase in the peak temperature up to 1170˚C, the effects of local melting around the γ-γ' eutectic and grain boundary were clearly evident in sample A (Fig. 14(b)). In a closer examination, the grain boundary liquid was observed to be associated with the constitutional liquation of Cr-Mo rich boride particles and Ni-Zr rich intermetallic compounds (Fig. 14(c)). As shown in Fig. 14(d), the most important factor in the formation of a crack in these conditions is melting the specimen and creating cracks under the tensile stresses, cooling it from a temperature of 1170˚C. However, the simulation for sample B at a temperature of 1170˚C did not show any local melting caused by the particles of boride and intermetallic. Only a few localized melting of γ' particles around the eutectic phase due to its incomplete dissolution were observed (Fig. 14(a)).

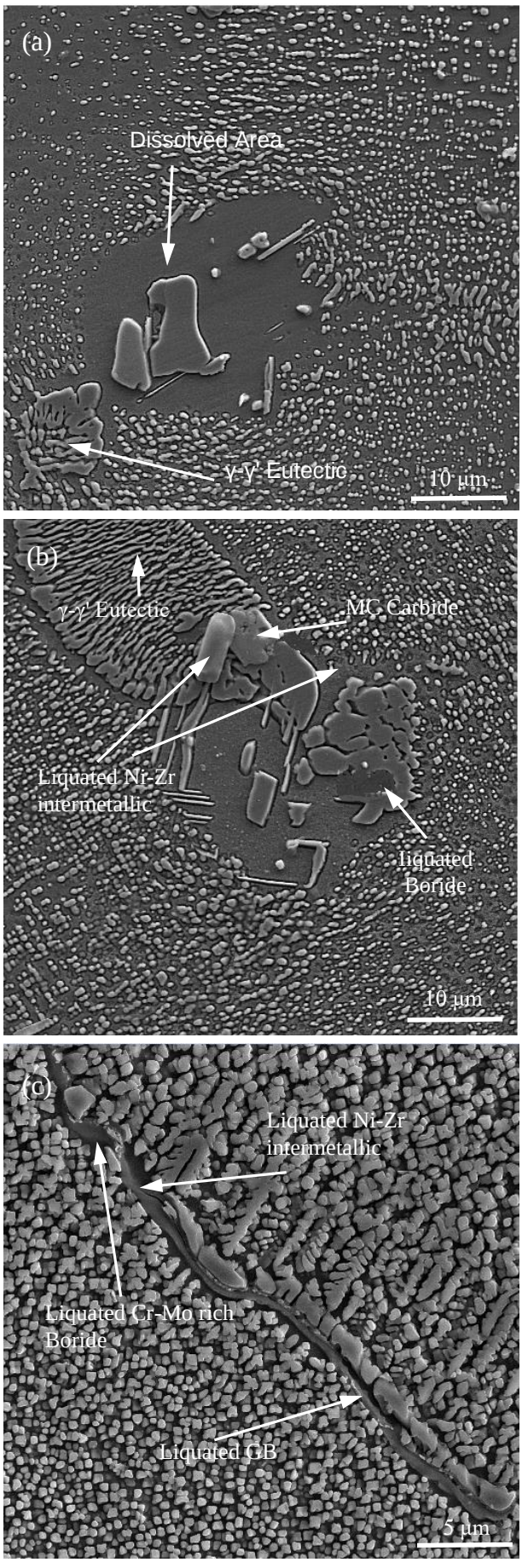

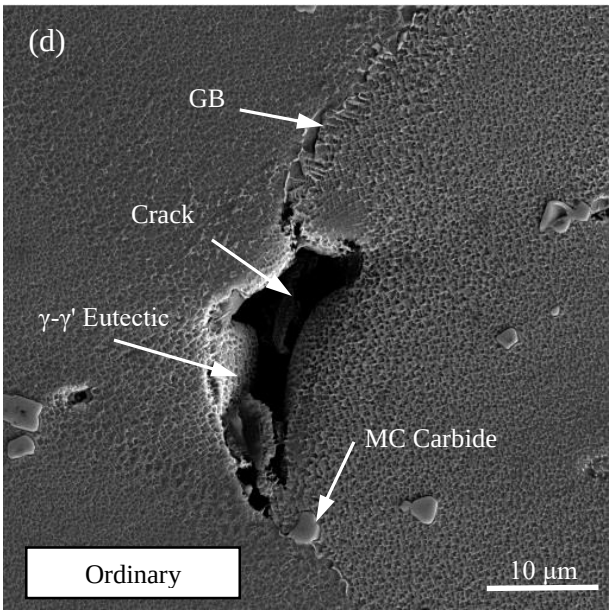

Fig. 14. Microstructure of Gleeble simulated sample at 1170˚C; (a) for sample B, (b), (c) and (d) for sample A.

Simulation at 1250˚C causes the partial melting of γ' particles in sample B. This is attributed to a higher temperature, 1250˚C, than the temperature of γ' dissolution. At this temperature, a slight melting of the MC carbide was also observed (Fig. 15).

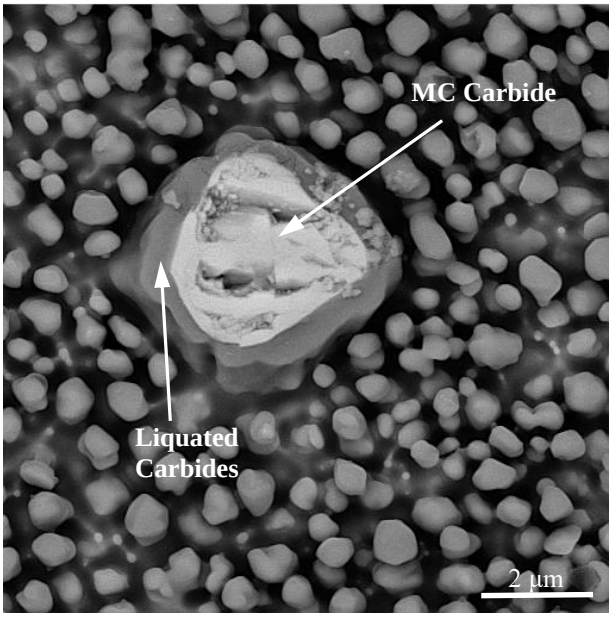

Fig. 15. Microstructure of Gleeble simulated sample at 1250˚C for sample B.

The above results were obtained while holding the alloy for 1 s at these temperatures. B specimen's results showed the partial melting of γ-γ' eutectic by holding a sample at 1170˚C for 3 s. This behavior is consistent with

the grain boundary liquation caused by the constitutional liquation of the second-phase Particles [33].

Generally, inter-granular liquation in nickel-based superalloys is poor hot ductility under tensile forces. Gleeble simulation was performed under tensile forces to investigate the hot ductility at the grain boundary. This time the samples were held at four temperatures for 0.1 s and then quenched with water. The results of the hot ductility test are presented in Fig. 16. Initially, the alloy appeared to be hot with high ductility, but the ductility dropped to a significantly low level at 1170˚C and approached zero at around 1250˚C. As earlier stated, widened grain boundaries were observed at the peak temperatures of 1170 and 1250˚C at which the alloy exhibited considerably poor ductility. By increasing the holding time from 0.1 to 3 s during the hot ductility test at 1250˚C, improvement in ductility from 3 to 19 pct was notably observed.

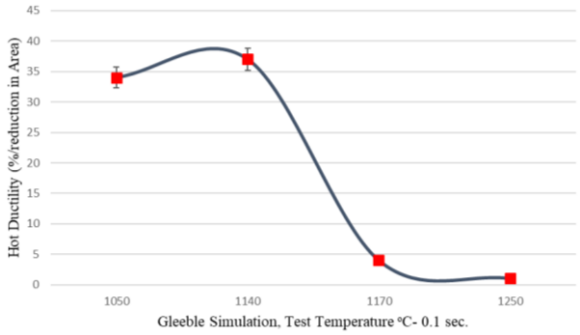

Fig.16. Variation of hot ductility of GTD-111 with peak temperature after a holding time of 0.1 s.

3.5. Microhardness results

According to Fig. 17, hardness of the weld metal in the autogenous joint is much higher than that of the base metals and HAZ, and consequently the weld metal in this state is very brittle. The reason is the presence of fine grains due to the high cooling rate of the weld as well as the presence of carbides which are distributed in the weld metal. Fine grains are a clear characteristic in laser welding. By passing from the weld metal and entering HAZ, hardness decreases and gets fixed at 502 VHN. The reason is the dissolution and disappearance of the precipitations during the welding [8]. In the base metal and HAZ, there are hardness fluctuations which are due to the presence of grains, grain boundaries, and intermetallic compounds at the inter-dendritic zones such as γ′, MC, and γ-γ′ eutectic microstructures. To conclude, the γ′ precipitation phase is responsible for the strengthening, especially for hardness in the precipitation-hardening nickel-based superalloys [34].

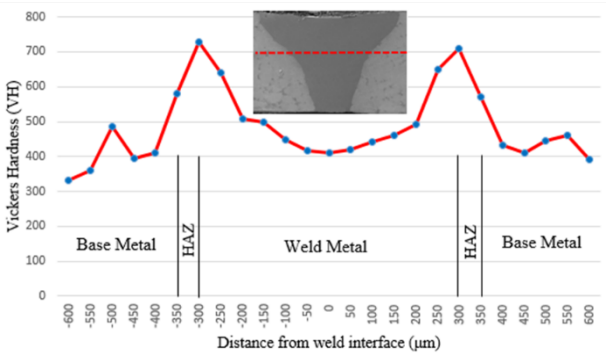

Fig. 17. Microhardness distribution in weld metal, HAZ and base metal.

3.6. Tensile testing

Figure 18 presents the tensile test results for the welded sample. As can be observed, the sample has been fractured in a zone outside the weld metal. This shows the achievement of a weld with good strength properties. The reason can be the size decrease and distribution mode of MC carbides in the weld metal (0.5 µm) compared with the carbide size in the base metal (1.5 µm), which results in more strength increase in the weld metal.

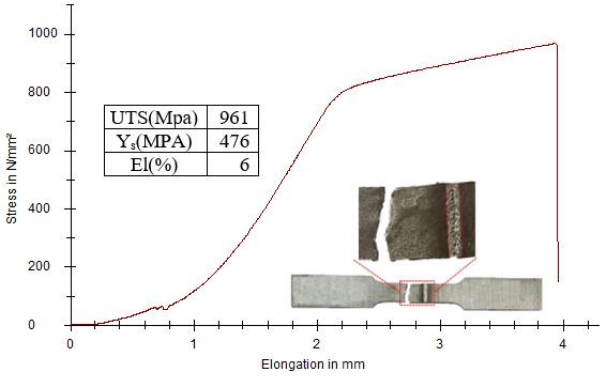

Fig. 18. Tensile stress-elongation curve of welded sample.

Figure 19(a) shows the fracture surface of the tensile test specimens. This figure shows that the tensile specimens have smooth fracture surfaces, a characteristic of a brittle inter-granular fracture [35].

This can be due to the presence of continuous cavities or inclusions or secondary particles which have precipitated at the grain boundaries as well as the decrease in the grain size and the way carbides have distributed in the weld metal in comparison with the base metal. Also, Fig. 19(b) shows a kind of inter-granular cracking and the role of MC carbide in crack formation. The brittle nature of MC carbides is the source of crack nucleation and growth at the inter-granular zones.

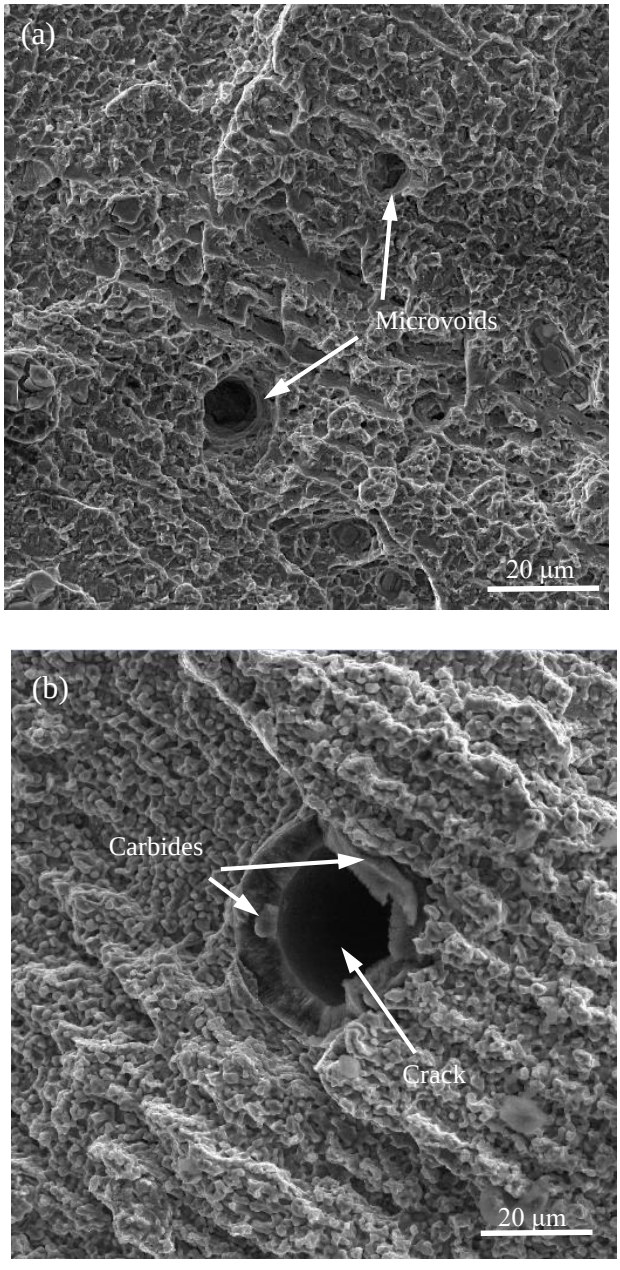

Fig. 19. Fracture cross section of the base metal: (a) intergranular fracture, (b) the presence of carbides around the crack.

4. Conclusions

In the present study, a GTD-111 nickel-based superalloy sheet with a thickness of 1 mm was welded using the pulsed Nd:YAG laser with a frequency of 20 Hz, pulse duration of 7 ms, and speed of 8.3 mms^{-1}. The results were obtained by the microstructural studies on the weld metal and HAZ as well as the mechanical behavior of the weld and also by the Gleeble physical simulation. The following results were achieved:

1. The weld metal structure consists of three zones, namely dendritic, cellular, and equiaxed, which are related to G and R values. By an increase in the GxR value, a higher cooling rate and consequently finer grains in the weld are obtained.
2. Solidification cracking was formed in FZ and propagated along the interdendritic region. The liquid film of solidification cracking was derived from the residual liquid metal caused by the segregation of Ti, Nb and Al elements in the interdendritic region at the last stage of solidification.
3. Epitaxial growth, observed in the weld structure, was due to the grain crushing at the boundary line.
4. EPMA analysis of the weld microstructure showed the segregation of Ti, Al, and Ta elements at the interdendritic zones due to K values of less than one, while W and Mo elements were distributed in the dendritic core zones. The rest of the elements were uniformly distributed in the weld zones.
5. Resolidified constituents were observed along the cracked grain boundaries in the HAZ of the welded cast GTD-111 alloy and it was concluded that one of the factors responsible for HAZ cracking in this alloy was grain boundary liquation.
6. Presence of a high amount of Ti in GTD-111 decreased the start temperature of the γ–γ' eutectic reaction and the dissolving temperature of γ'. This ended in the formation of liquation cracks at the grain boundaries as well as the development of γ' partial melting.
7. The cast specimen showed higher susceptibility to the constitutional liquation of terminal constituents than the standard solution annealed alloy at 1200˚C.

5. References

[1] M. Berahmand and S. A. Sajjadi, Morphology evolution of γ′ precipitates in GTD-111 Ni-based superalloy with heat treatment parameters, *International Journal of Materials Research* 104 (2013) 275-280.

[2] C.Yang, Y. Xu, Z. Zhang, H. Nie, X. Xiao, G. Jia, Improvement of stress rupture, life of GTD-111 by second solution heat treatment, *Materials & Design* 45 (2013) 308-315.

[3] M. Taheri, A. Salemi-Golezani, K. Shirvani, Effect of Aluminide coating on rapture behavior of Ni-based superalloy GTD-111 in high temperature, *Advanced Material Research* 457 (2012) 330-333.

[4] Gh. R. Razavi, J. Razavi, M. Taheri, M. Saboktakin, M 2013 Investigation mechanical properties and microstructure of pulsed Nd:YAG laser welding titanium, *International Journal of Materials and Mechanics Engineering* 2 No. 3 (2013).

[5] L. O. Osoba, R. K. Sidhu, O. A. Ojo, On preventing HAZ cracking in laser welded DS Rene 80 superalloy, *Materials Science and Technology* 27 (2011) 897-902.

[6] W. Wang, Li. Jiang, Li. Chaowen, Effects of post-weld heat treatment on microstructure and mechanical properties of Hastelloy N superalloy welds, *Materials Today Communications* 19 (2019) 230-237.

[7] R. A. Buckson, O. A. Ojo, Analysis of the influence of laser welding on fatigue crack growth behavior in a newly developed nickel-base superalloy, *Journal of Materials Engineering and Performance* 24 (2015) 353–361.

[8] M. Taheri, A. Halvaee, F. Kashani-Bozorg, Effect of Pre- and Post-weld Heat Treatment on Microstructure and Mechanical Properties of GTD-111 Superalloy Welds, *Metals and Materials International* 28 (2019).

[9] M. Montazeri, F. Malek-Ghaini, The liquation cracking behavior of IN738LC superalloy during low power Nd:YAG pulsed laser welding, *Material Characterization* 67 (2012) 65-73.

[10] M. Pang C. Y. Zheng, Microstructure study of laser welding cast nickel-based superalloy K418, *Journal of Materials Processing Technology* 207 (2008) 271-275.

[11] A. T. Egbewande, H. R. Zhang, R.K. Sidhu, O. A. Ojo, Improvement in laser weldability of INCONEL 738 superalloy through microstructural modification, *Metallurgical and Materials Transactions A* 40 (2009) 2694-2704.

[12] L. O. Osoba, R. G. Ding, O. A. Ojo, Microstructural analysis of laser weld fusion zone in Haynes 282 superalloy, Materials Characterization 65 (2012) 93-99.

[13] O. A. Ojo, N. L. Richards, M. C. Chaturvedi, Contribution of constitutional liquation of gamma prime precipitate to weld HAZ cracking of cast Inconel 738 superalloy, *Scripta Materialia* 50 (2004) 641-646.

[14] M. F. Chiang, C. Chen, Induction-assisted laser welding of IN-738 nickel–base superalloy, Materials Chemistry and Physics 114 (2009) 415-419.

[15] M. A. Rezaei, H. Naffakh-Moosavy, The effect of pre-cold treatment on microstructure weldability and mechanical properties in laser welding of superalloys, *Journal of Manufacturing Processes* 34 (2018) 339-348.

[16] M. Montazeri, F. Mmalek, O. A. Ojo, Heat Input and the Liquation Cracking of Laser Welded IN738LC Superalloy, *Welding Journal* 92 (2013) 258-264.

[17] M. R. Jelokhani-Niaraki, N. B. Mostafa Arab, H Naffakh-Moosavy, M Ghoreishi, The systematic parameter optimization in the Nd:YAG laser beam welding of IN 625, *International Journal of Advanced Manufacturing Technology* 84 (2016) 2537-2546.

[18] M. J. Torkamany, S. Tahamtan, J. Sabbaghzadeh, Dissimilar welding of carbon steel to 5754 aluminum alloy by Nd:YAG pulsed laser, *Materials & Design* 31 (2010) 458-465.

[19] M. Junaid, F. Nawaz Khan, K. Rahman, M. Nadeem Baig, Effect of laser welding process on the microstructure, mechanical properties and residual stresses in Ti-5Al-2.5Sn alloy, *Optics and Laser Technology* 97(2017) 405-419.

[20] B. K. Lee, W. Y. Song, D. U. Kim, Effect of Bonding Temperatures on the Transient Liquid Phase Bonding of a Directionally Solidified Ni-based Superalloy, GTD-111, *Metals and Materials International* 13 (2007) 59-65.

[21] M. Taheri, A. Halvaee, S. F. Kashani-Bozorg 2019 Effect of Nd: YAG pulsed-laser welding parameters on microstructure and mechanical properties of GTD-111 superalloy joint, *Materials Research Express* 6 (2019).

[22] Sindo Kou, Welding metallurgy, John wiley publication, second edition, 2003.

[23] G. Asala, O. A. Ojo, On post-weld heat treatment cracking in TIG welded superalloy ATI 718Plus, *Results in Physics* 6 (2016) 196-198.

[24] K. Han, H. Wang, L. Shen, B. Zhang, Analysis of cracks in the electron beam welded joint of K465 nickel-base superalloy, *Vacuum* 157 (2018) 21-30.

[25] F. Caiazzo, V. Alfieri, F. Cardaropoli, V. Sergi, Investigation on edge joints of Inconel 625 sheets processed with laser welding, *Optics and Laser Technology* 93 (2017) 180-186.

[26] T. E. Bower, H. D. Brody, M. C. Flemings, Measurement of solute redistribution in dendritic solidification, *AIME MET SOC TRANS* 236 (1996) 615-624.

[27] K. Simant-Bal, J. D. Majumdar, A. R. Choudhury, Effect of post-weld heat treatment on the tensile strength of laser beam welded Hastelloy C-276 sheets at different heat inputs, *Journal of Manufacturing Processes*, 37 (2019) 578-594.

[28] E. Scheil, Remarks on the crystal layer formation, *Zeitschrift für Metallkunde* 34 (1942) 70-72.

[29] J. N. Dupont, Microstructural development and solidification cracking susceptibility of a stabilized stainless steel, *Welding Journal* 52 (1999) 253-263.

[30] H. Moosavy, M. R. Aboutalebi, S. H. Seyedein, An analytical algorithm to predict weldability of precipitation-strengthened nickel-base superalloys, *Journal of Materials Processing Technology* 212 (2012) 2210-2218.

[31] O. A. Ojo, N. L. Richards, M. C. Chaturvedi, Liquid film migration of constitutionally liquated γ′ in weld HAZ of IN738LC superalloy, *Scripta Materialia* 51 (2004) 141-146.

[32] A. Dadkhah, A. Kermanpur, On the precipitation hardening of the directionally solidified GTD-111 Ni-base superalloy: Microstructures and mechanical properties, *Materials Science and Engineering: A* 658 (2017) 79-86.

[33] J. J. Pepe, W. F. Salvage, Weld. J 46 (1967) 411s-26s.

[34] C. Yang, Y. Xu, Z. Zhang, H. Nie, Z. Shen, Improvement of stress-rupture life of GTD-111 by second solution heat treatment, *Materials & Design* 45 (2013) 308-31.

[35] M. Paidar, A. Khodabandeh, M. Lali Sarab, M. Taheri, Effect of welding parameters (plunge depths of shoulder, pin geometry, and tool rotational speed) on the failure mode and stir zone characteristics of friction stir spot welded aluminum 2024-T3 sheets, *Journal of Mechanical Science and Technology* 29 (2015) 4639-4644.

تحلیل و بررسی تشکیل ترک در سوپرآلیاژ پایه نیکل جوشکاری شده به روش لیزر Nd:YAG پالسی

مرتضی طاهری[۱]، ایوب حلوایی[۲]، سید فرشید کاشانی بزرگ[۲]، مسلم پایدار[۱]

۱- بخش مهندسی مواد، واحد تهران جنوب، دانشگاه آزاد اسلامی، تهران، ایران.
۲- دانشکده مهندسی متالورژی و مواد، دانشکده فنی، دانشگاه تهران، تهران، ایران.

چکیـــده

در پژوهش حاضر، جوش پذیری سوپرآلیاژ پایه نیکلی GTD-111 توسط لیزر Nd:YAG پالسی با متوسط توان ۲۵۰ w مورد مطالعه قرار گرفت و همچنین ارزیابی و خصوصیات ترک نیز مورد بررسی قرار گرفت. ترک انجمادی در ناحیه فلز جوش و همچنین ترک ذوبی بین دانه ای در ناحیه متاثر از حرارت مشاهده گردید. علت تشکیل ترک انجمادی، جدایش عناصر تیتانیوم، نایوبیوم و آلومینیوم در نواحی بین دندریتی که آخرین مذاب باقیمانده قبل از انجماد در آنجا وجود دارد، اتفاق افتاده است. همچنین ترک ذوبی در ناحیه متاثر از حرارت همراه با ذوب ترکیبی فاز γ'، کاربید MC و بوریدهای غنی از کروم بود. تیتانیوم مهمترین عامل در تشکیل ترک ذوبی در ناحیه متاثر از حرارت بود که از طریق کاهش دمای شروع واکنش یوتکتیک $\gamma-\gamma'$ و افزایش دمای انحلال فاز γ' حساسیت به تشکیل ترک را افزایش می دهد. آنالیز شیمیایی لبه های ترک در HAZ، حضور مقدار بالایی از عناصر Ti و Al را نشان می داد که به ذوب جزئی γ'، نسبت داده می شود. شبیه ساز فیزیکی Gleeble نشان داد که در نمونه های ریختگی، تشکیل مذاب به طور چشم گیری در دمای پایین تری نسبت به نمونه های عملیات حرارتی شده در دمای ۱۲۰۰°C شروع می شود که این موضوع به فازهای بورایدی و بین فلزی نسبت داده می شود که در شرایط عملیات حرارتی در دمای ۱۲۰۰ °C در زمینه حل شده بودند. تشکیل دانه های ریز به دلیل نرخ سرد شدن بالای جوش و همچنین تشکیل کاربیدهای پراکنده در نواحی جوش و متاثر از حرارت، باعث افزایش سختی در حدود ۱۳۰ ویکرز نسبت به فلز پایه شده است.

واژه‌های کلیدی: سوپرآلیاژ GTD-111، لیزر Nd:YAG، ترک انجمادی، ترک ذوبی، ذوب مرزدانه ای، ضریب جدایش، شبیه سازی Gleeble